Production of hydrogen and carbon nanotubes from methane pyrolysis using a multi-pass floating catalyst chemical vapour deposition reactor with process gas recycling

Jack Peden[1]* jdp62@cam.ac.uk, James Ryley[2] jbr40@cam.ac.uk,
Jeronimo Terrones[1,2] jeronimo@q-flo.com, Fiona Smail[1] frs25@cam.ac.uk,
James A. Elliott[3] jae1001@cam.ac.uk, Alan Windle[3] ahw1@cam.ac.uk,
and Adam Boies[4] aboies@stanford.edu

[1] University of Cambridge, Department of Engineering, Trumpington Street, Cambridge, CB2 1PZ, United Kingdom

[2] Q-Flo Limited, 1st Floor One Suffolk Way, Sevenoaks, Kent, England, TN13 1YL, United Kingdon

[3] University of Cambridge, Department of Materials Science and Metallurgy, 27 Charles Babbage Rd, Cambridge, CB3 0FS, United Kingdom

[4] Mechanical Engineering, Stanford University, Building 530, 440 Escondido Mall, Stanford, CA 94305-3030, United States

* Corresponding Author, email: jdp62@cam.ac.uk

September 2025

Abstract

Converting natural gas into hydrogen and solid carbon materials using methane pyrolysis presents a promising opportunity to produce sustainable fuels and materials. Hydrogen and bulk carbon nanotube (CNT) production via methane pyrolysis have been demonstrated independently, but concurrent production from the same reactor remained elusive. Here, we present a multi-pass floating catalyst chemical vapour deposition (FCCVD) reactor that converts methane into hydrogen and CNT aerogel. Whereas prior FCCVD CNT production consumed hydrogen, the multi-pass reactor recycles the carrier gas to eliminate any hydrogen input. This results in a net output of 85 vol% hydrogen alongside CNT aerogel, and a 446-fold increase in molar process efficiency. Further, the demonstrated use of biogas to produce CNT aerogel enables potential net sequestration of CO_2 from the atmosphere. The results of this study are extrapolated to a pilot-scale reactor, using data gathered at a commercial facility, to consider challenges and opportunities associated with scale-up.

Main

Converting natural gas into hydrogen and solid carbon using methane pyrolysis presents a method to produce sustainable fuels and materials, utilising hydrocarbon feedstocks that would otherwise be burned and produce greenhouse gas emissions. Hydrogen is sought as an energy vector for hard to electrify sectors, and already plays a vital role as a precursor for artificial fertiliser production and other industries [1, 2, 3]. Today's hydrogen production of $\sim$100 Mt y^{-1} contributes 2-3% of global annual greenhouse gas emissions [4, 5]; alternative, sustainable modes of production are needed. Additionally, >10% of greenhouse gas emissions can be attributed to the production of materials, particularly steel (7.2%) and concrete (3%) [6]. Alternative materials with reduced embedded emissions are also key to enabling the transition to a low greenhouse gas economy.

Methane pyrolysis decomposes natural gas into "turquoise" hydrogen and solid carbon by the reaction

$$CH_4(g) \rightarrow C(s) + 2H_2(g). \tag{1}$$

The pyrolysis reaction is endothermic and endergonic ($\Delta H^\circ = 37.4$ kJ mol(H$_2$)$^{-1}$ and $\Delta G^\circ = 25.4$ kJ mol(H$_2$)$^{-1}$) [7], yet requires less energy than hydrogen production by water splitting ($\Delta H^\circ = 286$ kJ mol(H$_2$)$^{-1}$) or steam methane reforming (63 kJ mol(H$_2$)$^{-1}$) [8, 9] with the added benefit of producing solid carbon that can serve as a useful material rather than CO_2 which requires further energy for capture and storage. The solid carbon can take the form of graphite or carbon nanomaterials which provide a material revenue stream [10]. Bulk carbon nanotube (CNT) materials are exceptionally versatile [11], with fibres possessing high electrical conductivity (5 MS m^{-1}) [12], thermal conductivity (770 W m^{-1} K^{-1}) [13] and low density (1-2 kg m^{-3}) [14]. CNT fibres have undergone a doubling of strength every three years [15], culminating in a fibre with the highest recorded tensile strength, over 8 GPa, produced in 2024 (Fig. 1b) [16]. Methane pyrolysis can be CO_2-negative if bio-derived methane precursor is used, taking atmospheric carbon sequestered by photosynthesis and converting it into solid materials (Fig. 1c) [5]. Methane pyrolysis, outlined in Fig. 1, thus provides an appealing technology to produce low-CO_2-intensity and energy-intensity hydrogen alongside functional carbon materials that sequester rather than release carbon [5, 17, 18].

The direct production of CNT mats and fibres from methane has been achieved using floating catalyst chemical vapour deposition (FCCVD) reactors [19]. CNT production using this process has hitherto consumed hydrogen, in the form of dilution gas to suppress unwanted side-reactions, rather than produce it [20]. Hydrogen and CNTs have been produced simultaneously in fluidised-bed systems [21, 22, 23, 24], and at least one patent exists for such a system [25]. However, these systems produce CNT powders, not structural materials. The largest powdered carbon market appears to be carbon black, but at 18 Mt y^{-1} [26], this is 100× smaller than the rate at which carbon is produced in the form of natural gas (1.9 GT yr^{-1}) [27]. Structural materials, like steel with a market of 1.6 GT yr^{-1}, are among the few commodities used on the same scale as hydrocarbons and thus present the most viable markets into which pyrolytic carbon materials could be absorbed [27].

In this study, we demonstrate the co-production of turquoise hydrogen and CNT mat using a multi-pass (MP) FCCVD reactor that recycles process gas. This removes the need for an exogenous hydrogen supply during steady state operation. The multi-pass process is demonstrated with pure methane and methane contaminated with 33 vol% CO_2. The latter simulates unrefined bio-derived methane such as biogas or landfill gas [28], which unlocks the potential for a carbon-negative process [5]. We investigate the differences between the multi-pass reactor and tradition single-pass (SP) reactor, in terms of process efficiencies and mass conversion, and characterise the resulting CNTs. We then apply our findings to data obtained from a pilot-scale reactor operated by industrial CNT producers to extrapolate the effects of the multi-pass process on larger reactors.

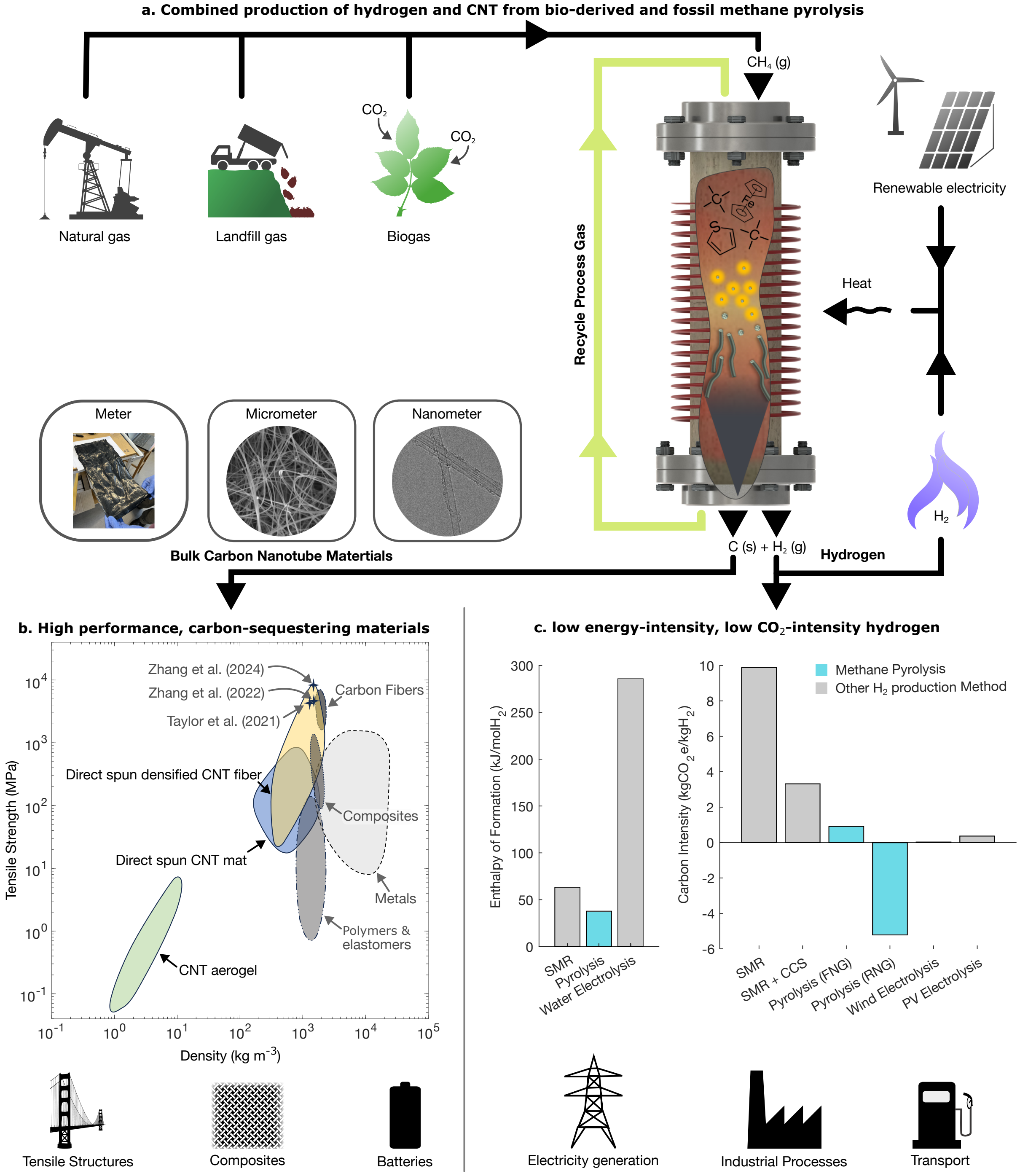

Figure 1: Methane pyrolysis to produce hydrogen and bulk CNT materials from methane. (a) Methane (CH_4 (g)), obtained from natural gas, landfill gas, or biogas, is decomposed inside a hot reactor into hydrogen gas (H_2 (g)) and solid carbon (C (s)) catalytically grown into carbon nanotubes that are collected from the reactor as aerogel. (b) CNT materials possess exceptional tensile strength finding potential applications in tensile and composite materials, and existing additive markets like batteries [47, 16, 11, 15, 48, 49]. (c) Hydrogen production by methane pyrolysis is both energy efficient and has low CO_2-intensity, providing a clean fuel and precursor for electricity generation, industrial processes and transport [8, 9, 5]. Icons in this figure are from from Openclipart.org, adapted and reproduced under Creative Commons Zero license.

Multi-Pass Reactor Configuration

During steady state operation, the multi-pass reactor is a quasi-closed loop with ∼99 vol% of process gas circulating inside the reactor, making multiple passes of the high-temperature reaction zone. A relatively small quantity of precursors (methane and catalyst) are added to the reaction mixture before each pass of the furnace, producing CNT aerogel and hydrogen which are removed from the reactor. Figure 2a is a schematic of the multi-pass reactor operating in steady-state where 1785 SCCM of process gas is recycled from the exhaust back to the injector. This gas consists primarily of hydrogen (H_2), hydrocarbons (C_xH_y) and hydrogen sulphide (H_2S). An additional 15 SCCM flow of methane and catalyst precursors (ferrocene, $C_{10}H_{10}Fe$, and thiophene, C_4H_4S) is added to the recycled gas prior to furnace injection.

Flowing through the furnace, the precursors are heated to ∼1300 °C causing the methane to undergo pyrolysis which produces hydrogen and C_2 species (primarily acetylene and ethylene) in the presence of nucleating iron-sulfur nanoparticles [29, 30]. Catalyst particles nucleate and grow CNTs [31] from the pyrolysis species, these then agglomerate into bundles and form an interconnected aerogel [32, 33] which is extracted from the gas stream onto a rotating roller within the collection chamber. Figure 2b shows the aerogel exiting the reaction tube and being wound onto the roller, which collects the CNTs as a mat (Fig. 2c) or fibre. The process gases leave the collection chamber and 1785 SCCM of gas is recycled back to the injector for another pass of the reactor. An effluent flow of 22.5 SCCM containing 84.7 vol% H_2 was measured during steady state operation, corresponding to 19.1 SCCM of H_2 production and 54% hydrogen production efficiency. Hydrogen concentration could be increased with pressure swing absorption (Supplementary Figure 1), as is done in steam methane reforming processes [9]. See Supplementary Note 1 and Supplementary Figure 2 for details on how steady state is achieved and Supplementary Figure 3 and Supplementary Note 2 for more details on steady state hydrogen production. Figure 3 is a detailed schematic of the reactor used in this study, and Supplementary Figure 4 is a picture of the reactor.

In addition to enabling combined production of CNTs and turquoise hydrogen, the multi-pass reactor proffers a significant efficiency improvement over a tradition single-pass reactor represented in Fig. 2d. Here, reactants exit the reactor after a single pass of the furnace resulting in a waste stream, comprised of unreacted gases and solid losses, that accounts for 99 wt% of the mass throughput at lab-scale. The multi-pass process, represented in Fig. 2e, reduces the size of the waste stream to 6 wt% by recycling 92 wt% of the total mass flow. By utilising recycled hydrogen in the multi-pass process, the exogenous hydrogen supply is completely removed resulting in a much smaller input stream in Fig. 2e compared to Fig. 2d. By recycling rather than consuming dilution hydrogen, the hydrogen produced by pyrolysis in the multi-pass reactor can be collected as a secondary product stream. Overall, these developments give a 33-fold reduction in Waste:Product between the lab-scale single-pass and multi-pass processes, from 99:1 (single-pass) to 3:1 (multi-pass). Further improvements come with scale-up to a Pilot process as discussed around Fig. 6.

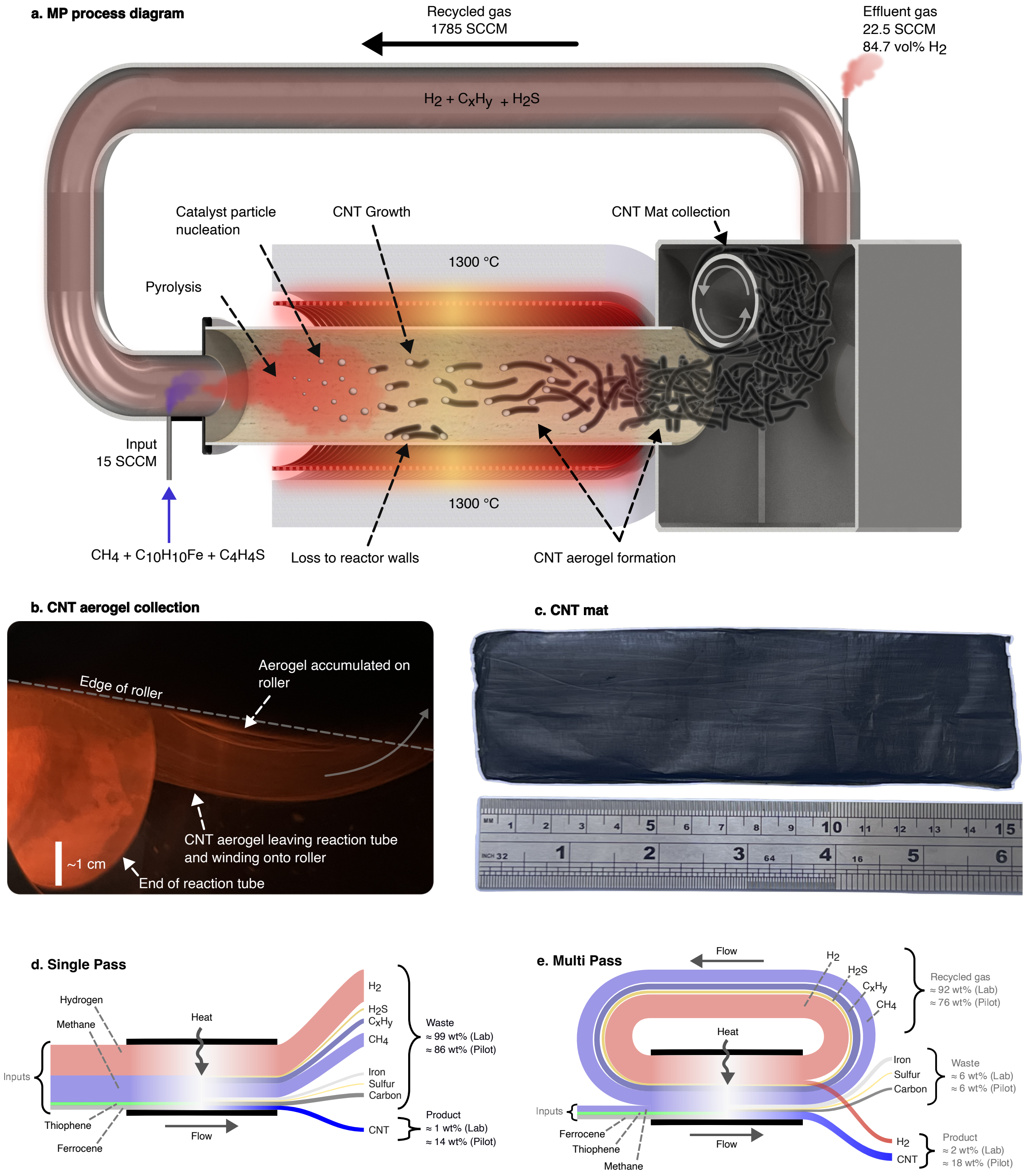

Figure 2: Configuration of the multi-pass reactor developed in this study. (a) Schematic of the reactor, showing ~99 vol% recycled process gas, CNT production and hydrogen effluent flow leaving the reactor. (b) Photograph of CNT aerogel leaving the reaction tube and winding onto the collection roller. (c) Photograph of a mat made of multiple layers of CNT aerogel after removal from the reactor. Conceptual models showing mass flows in the (d) single-pass and (e) multi-pass processes. The multi-pass process is primarily composed of recycled gas passing repeatedly through the reactor in a loop, resulting in smaller input and waste streams. The magnitudes of flows are not drawn to scale and the relative weight % of each stream is indicated for the lab scale process detailed in Fig. 4 and the pilot-scale process detailed in Fig. 6.

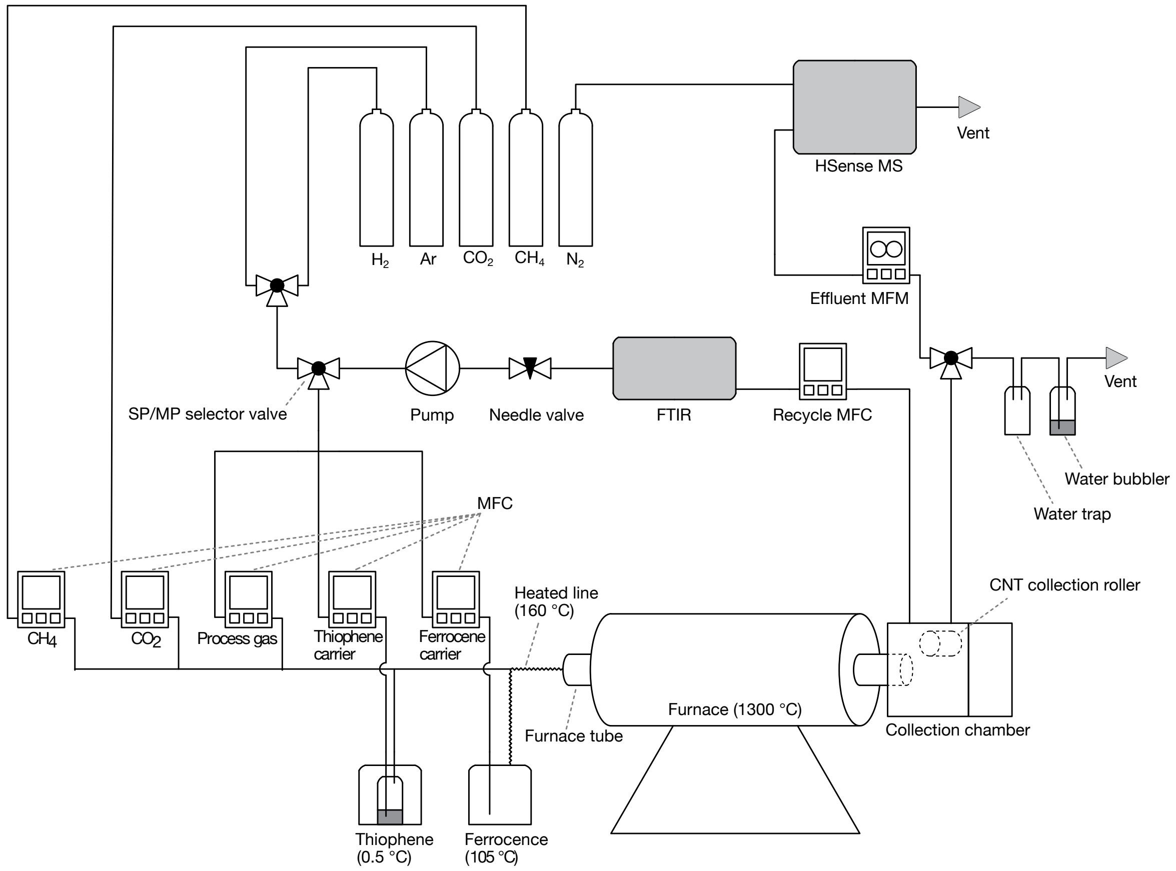

Figure 3: Schematic of the reactor used in this study. The same reactor can be operated in single-pass (SP) and multi-pass (MP) configurations, depending on the position of the SP/MP selector valve. Instruments used to characterise the process gas, including Fourier transform infrared spectrometer (FTIR), mass spectrometer (MS), and mass flow meter (MFM) are also shown. See Methods section for more detail.

Mass Conversion in the Lab-Scale Process

Figure 4 gives a detailed breakdown of the mass conversion taking place inside the single-pass and multi-pass reactors. The inputs on the left of Fig. 4a and Fig. 4b represent inputs shown on the left of Fig. 2d and Fig. 2e, respectively (recycled gases are not included). By recycling unreacted gases in the multi-pass reactor, throughput is reduced from 16.38 g h^{-1} to 1.15 g h^{-1}, yet the CNT production is increased from 0.13 g h^{-1} to 0.17 g h^{-1}.

The waste produced in the multi-pass process (0.88 g h^{-1}) is significantly lower than the single-pass process (16.25 g h^{-1}). The single-pass waste stream in Fig. 4a is mostly hydrogen, but also contains >70% of the methane supply, which leaves unreacted, along with a further 10% of the carbon input in the form of hydrocarbon pyrolysis products (C_xH_y). By recycling these gases, the multi-pass reactor only needs enough methane input to "top up" the carbon that is consumed in each pass of the furnace. The multi-pass process thus removes the need for an exogenous H_2 input, enables a 10-fold reduction in the methane input, and a 50% reduction in thiophene input (Fig. 4). The multi-pass process increases the amount of product from 0.13 g h^{-1} to 0.27 g h^{-1} (140 g h^{-1} m^{-3} to 293 g h^{-1} m^{-3}), owing largely to the additional H_2 product stream. The solid carbon loss is reduced 2-fold in the multi-pass process, from 1.1 g h^{-1} to 0.57 g h^{-1}, but 71% of the carbon is still lost.

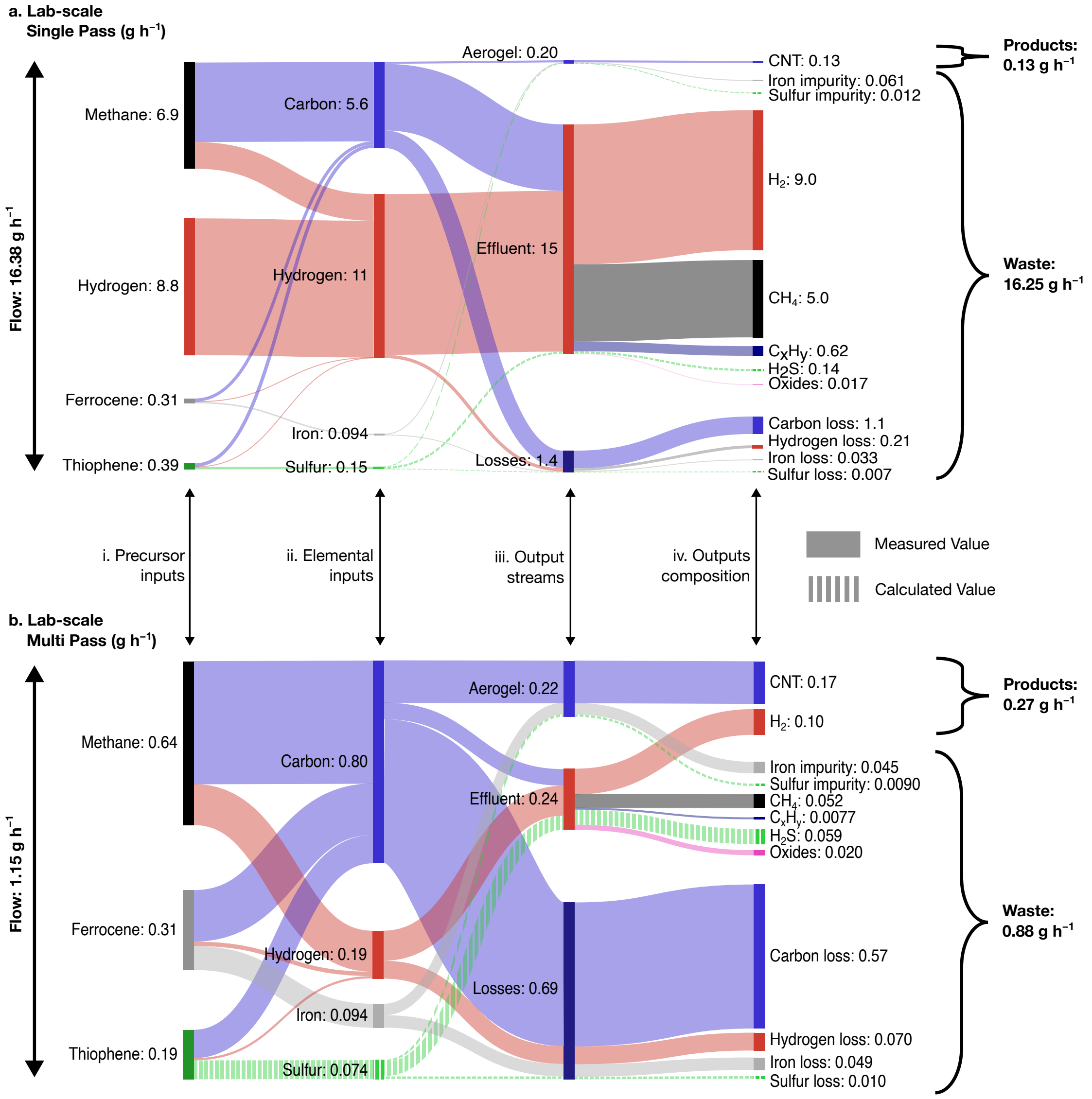

Figure 4: Mass conversion in g h^{-1} in the (a) lab-scale single-pass and (b) multi-pass processes. Sankey diagrams represent the flow of mass into and out of the reactor during a single-pass: in the single-pass process (a), this represents all the mass flowing through the reactor; in the multi-pass process (b), this only represents mass added to and removed from the reactor, not the large flow of gas that is continually recycled. The diagrams show the flow of mass from (i) precursor inputs on the left, to (ii) elemental inputs, to (iii) output streams, to (iv) a breakdown of the chemical composition of output streams on the right. Solid fills indicate measured data, striped fills indicate calculated values. The mass of ”oxides” in effluent flow, formed from fugitive oxygen, includes only the carbon and hydrogen components. See the methods section for detailed calculations.

Single-Pass and Multi-Pass Performance

Both single-pass and multi-pass reactors were run with concentrated (SP, MP) and dilute (SP2, MP2) precursor mixtures. An additional mixture of concentrated precursors with 33 vol% CO_2 impurity in the methane (MPbio) was also tested to simulate unrefined bio-derived methane. Supplementary Table 1 details these reaction mixtures, Fig. 5 and Table 1 summarise the results of these experiments (methods describe calculations). Figure 5a compares the performance of each process relative to the concentrated single-pass (SP) process. Moving from single-pass to the dilute single-pass (SP2) process there is a decrease in CNT mass production, carbon yield, and molar efficiency of 40 - 70%; with fewer precursors inside the reactor, less conversion takes place. At the same time, CNT properties increased in the dilute process, most notably Raman I_G:I_D ratio (3.8×) and electrical conductivity (17×). The need to balance throughput with CNT properties is reported in the literature and appears to be a caveat of FCCVD reactors [34, 35].

Both concentrated and dilute multi-pass processes (MP and MP2) show clear efficiency improvements in Fig. 5a, with 7.7 - 8.7× increase in carbon yield and 42 - 53× increase in molar carbon efficiency compared to the concentrated single-pass process. Whereas the dilute single-pass process sees a drop in efficiency compared to the concentrated single-pass, the dilute multi-pass still proffers a significant efficiency improvement, though its CNT production rate is decreased by 42%. When the additional hydrogen product stream from the concentrated multi-pass process is considered, its overall molar process efficiency is increased to 44.69%: 446× higher than the concentrated single-pass process which operates at 0.1% molar efficiency, typical for lab-scale FCCVD reactors [20]. Moving from single-pass to multi-pass proffered an increase in CNT mass production rate 25% in the concentrated case, and 67% in the dilute case.

The introduction of CO_2 impurities into the multi-pass process (MPbio) reduced its efficiency compared to running on pure methane. It still exhibited a 4-fold and 32-fold increase in carbon yield and molar carbon efficiency compared to the single-pass process, but suffered a 25% reduction in CNT mass production. The reduced efficiency and productivity of the MPbio process is attributed to CO_2 oxidising carbon to form CO which acts as a detrimental carbon sink. See Supplementary Note 3 for more details, and Supplementary Figure 5 for oxide concentrations in the process gas.

Comparing Raman spectra in Fig. 5b, material produced with concentrated reaction mixtures show a range of I_G:I_D ratios (1.4 - 1.8), while the dilute material show very similar I_G:I_D ratios of $\sim$6. TGA curves in Fig. 5c show the multi-pass processes produce material with less iron impurity than their single-pass counterparts, evidenced by the $\sim$ 30% smaller residual mass. Conversely, the MPbio material contains 15% more iron than the single-pass material. The material produced with dilute recipes (SP2, MP2) shows more mass loss at high temperature (>600°C), indicating the presence of CNTs with more graphetisation and fewer defects [23]. The material produced under dilute conditions is significantly more electrically conductive (>10×) than the concentrated material and also more dense. The dilute single-pass material exhibits the highest electrical conductivity (63669 S m^{-1}), density (273 kg m^{-3}), and specific conductivity (233.2 S m^{-2} kg^{-1}).

Structural differences are visible in TEM images of the CNT material, shown in Fig. 5d-h. Moving from concentrated (Fig. 5d-f) to dilute recipes (Fig. 5g,h) the CNTs appear longer, forming more coherent networks. In particular, the dilute single-pass material (Fig. 5g) shows dense bundles with diameters of $\sim$100 nm containing many CNTs, possibly explaining the high density and electrical conductivity of this material. Comparing the concentrated multi-pass material in Fig. 5e to the single-pass material Fig. 5d, there is a visible reduction in the number and size of iron nanoparticles, corroborating the lower residual mass in TGA. The CNTs in the concentrated multi-pass and MPbio material appear shorter than the CNTs in the single-pass material, and all three samples were composed of multi-wall CNTs with $\sim$10 nm diameter. The CNTs produced with dilute recipes (SP2, MP2) are also multi-walled, albeit with fewer walls. Many CNTs in the MPbio material (Fig. 5f) exhibit ”herringbone” walls where the graphite planes are diagonal to the axis of the CNTs, possibly a result of the additional CO_2 impurity.

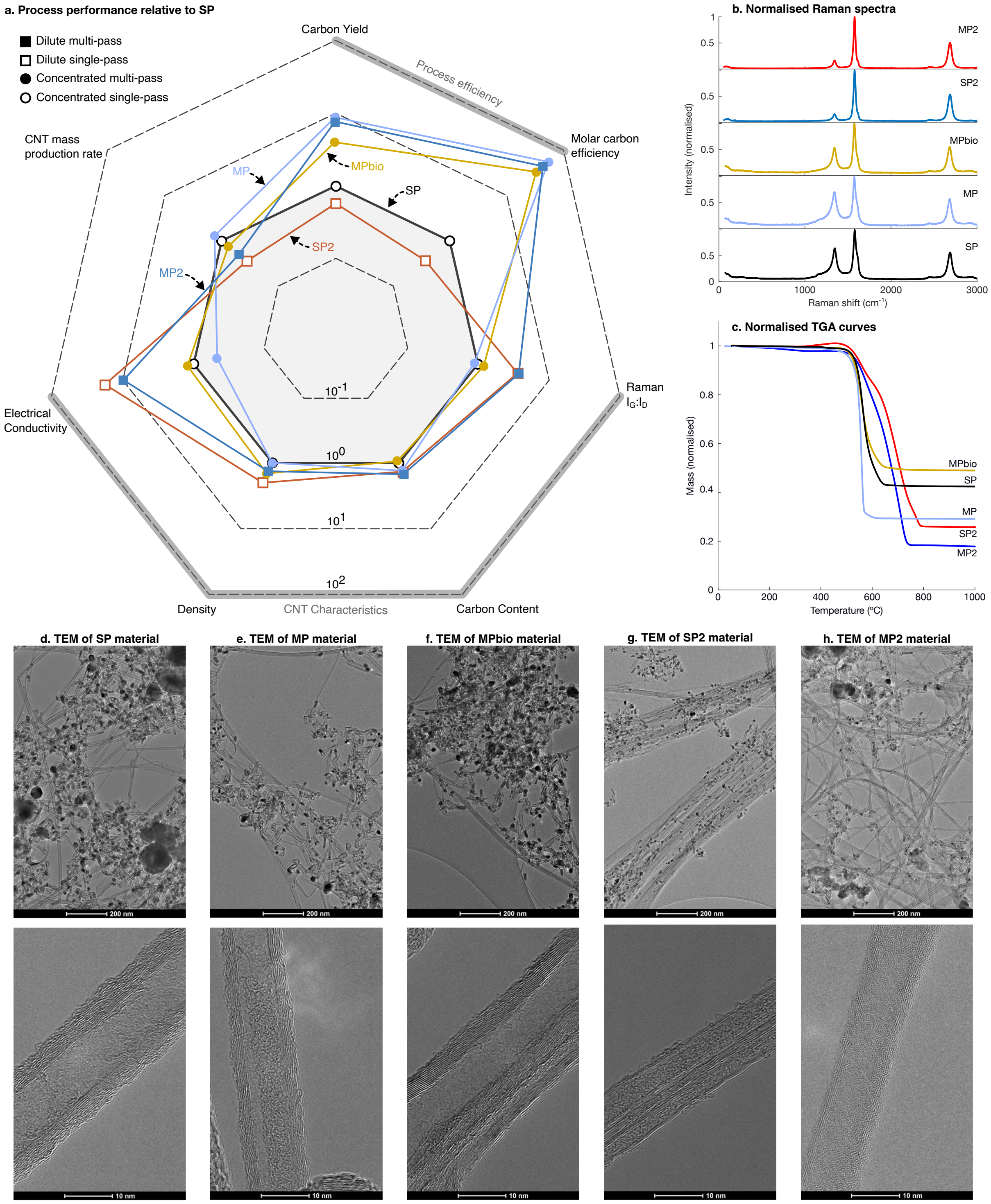

Figure 5: Comparison of single-pass and multi-pass reactors, in terms of process performance and CNT product. Five operating conditions are shown: concentrated single-pass (SP), concentrated multi-pass (MP), concentrated multi-pass with biogas (MPbio), dilute single-pass (SP2), and dilute multi-pass (MP2). (a) Comparison of process performance metrics and material characteristics, plotted on a logarithmic scale normalised by SP process performance. (b) Normalised Raman spectra, (c) normalised TGA curves, and (d-h) TEM images of CNT material produced by each process.

Mass Conversion in the Pilot-Scale Process

To assess the scale-up implications of the multi-pass process, we collected data from a pilot-scale single-pass reactor operated by Tortech Nano Fibers to construct the Sankey diagram in Fig. 6a. The pilot reactor operates at higher CNT production rate (30 g h^{-1}), volumetric productivity (3.4 kg h^{-1} m^{-3}), and carbon yield (60%) than the lab-scale reactor. The solid carbon loss is 5.9 g h^{-1}, one fifth of the size of the CNT product stream. However, the pilot single-pass process in Fig. 6a is dominated by the large hydrogen waste stream, having net H_2 loss through the process.

Applying reaction efficiencies of the multi-pass process to the pilot-scale reactor indicates that a pilot-scale multi-pass process could achieve efficient conversion of methane into CNTs and hydrogen. Figure 6b represents a pilot-scale reactor running in the multi-pass configuration, producing 30 g h^{-1} of CNTs. The reduction in waste combined with the increase in product make the multi-pass process 57× more efficient than the single-pass process on a molar basis. The dominant carbon loss stream exhibited by the lab-scale multi-pass process in Fig. 4b is reduced at pilot scale, becoming secondary to the CNT and hydrogen product streams in Fig. 6b. Overall, the process outputs are 75% product by mass, with the process producing CNTs and hydrogen in a 3:1 mass ratio at a rate of 4.5 kg m^{-3} h^{-1}, with 88% hydrogen production efficiency. While this is a significant improvement in efficiency compared to the pilot single-pass process, the pilot multi-pass process still outputs 25% waste by mass meaning further improvements can be pursued scaling from pilot to industrial reactors.

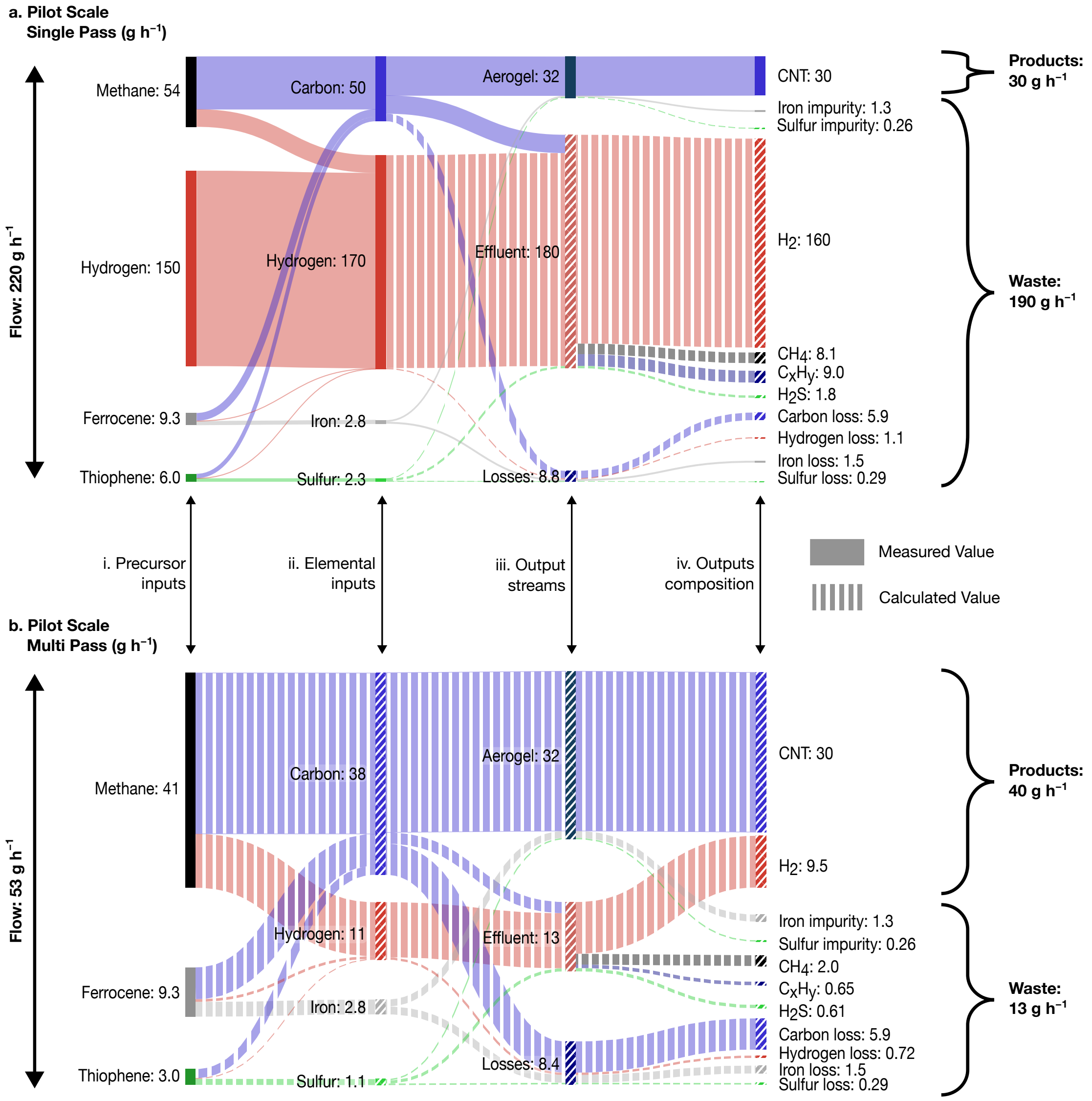

Figure 6: Mass conversion in g h^{-1} (a) pilot-scale single-pass and (b) a modelled pilot-scale multi-pass processes, with the multi-pass process demonstrating much more efficient precursor conversion. Sankey diagrams show the conversion of mass, in g h^{-1}, from (i) precursor inputs and (ii) elemental inputs, to (iii) output streams, and (iv) a breakdown of the chemical composition of output streams. Solid fills indicate measured data, striped fills indicate calculated values. See the methods section for more detail on the construction of these diagrams.

Multi-pass FCCVD compared to other pyrolysis technologies

The single-pass processes used here exhibit relatively low molar carbon efficiency (0.04 - 0.1%) and carbon yield (1.4 - 2.4%), yet the multi-pass processes are able to achieve much higher molar carbon efficiency (4.2 - 5.5%) and carbon yield (18.2 - 20.8%), as shown in Fig. 7a. Scaling the reactor up with the Pilot single-pass process achieves a carbon yield of 60%: much higher than lab-scale processes. The Pilot multi-pass process model predicts carbon yield and molar carbon efficiency of 79%, along with hydrogen volumetric productivity of 1.1 kg m^{-3} h^{-1}, approaching the efficiencies of fluidised bed systems [26], as shown in Fig. 7b. Supplementary Figure 6 compares the multi-pass reactor to other ”hydrogen-first” pyrolysis reactors.

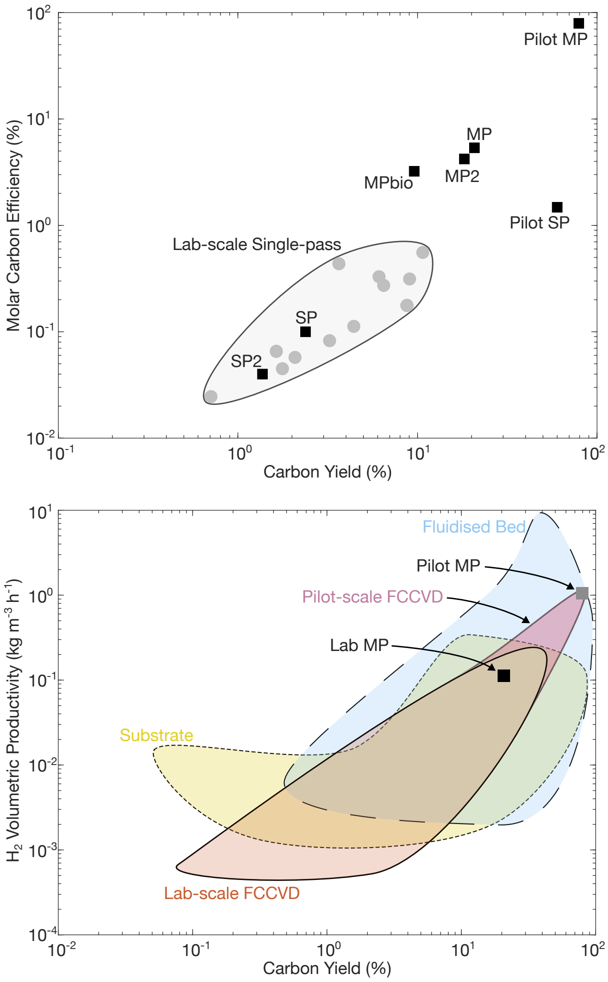

Figure 7: Comparison of the multi-pass and single-pass process performance to literature data. (a) CNT production efficiency in terms of molar carbon efficiency and carbon yield compared to data for lab-scale FCCVD reactors presented by Weller at al. [20]. (b) H_2 productivity and carbon mass conversion compared to data presented by Glerum & Boies [26] for FCCVD, substrate and fluidised bed CNT reactors.

Discussion

This study demonstrates that an FCCVD CNT reactor can operate in a multi-pass configuration with ∼99% recycled process gas, requiring no exogenous hydrogen supply. The multi-pass reactor produced H_2 with 84.7 vol% purity and CNT aerogel, both were continuously extracted from the reactor. Compared to a conventional single-pass FCCVD reactor, the multi-pass reactor demonstrated an 8.7-fold improvement in carbon yield and 446-fold improvement in molar process efficiency. These efficiency gains are accompanied by comparatively small changes to the characteristics of the CNT aerogel. The dilute multi-pass recipe produced CNTs with Raman $I_G/I_D = 6$, comparable to the CNTs used by Zhang et al. (2024) [16] to create a fibre with tensile strength of 8 GPa. Applying these findings to data collected from a commercial single-pass CNT reactor, we calculate that a pilot-scale multi-pass reactor could produce CNTs and hydrogen in a 3:1 mass ratio, with 75% of the mass throughput converted into useful products.

The co-production of CNTs and hydrogen has been reported previously using fluisided bed reactors [21, 22, 23, 24]. These processes require periodic removal of CNTs and regeneration of the catalyst, so the FCCVD reactor's ability to continuously extract CNTs and synthesise fresh catalyst is advantageous. However, fluidised bed reactors utilise more concentrated methane feedstock (25-100 vol% CH_4) than FCCVD reactors (5-10 vol% CH_4), allowing greater hydrogen productivity. Fluidised bed reactors are characteristic of "hydrogen-first" processes like molten metal, thermal pyrolysis, and plasma pyrolysis reactors [36, 18, 10, 17]. These reactors enable high-productivity synthesis of turquoise hydrogen from concentrated methane feedstocks, while producing relatively low-value solid carbon. The fluidised bed reactors typically produce CNTs of large diameter (>50 nm) and low I_G:I_D ratio (≈ 1) which are collected in powder form. Recent innovations in rotary kiln reactors enable the continuous synthesis of CNTs, potentially with lower diameters than those from fluidised bed reactors, but the CNTs are still harvested as powder [25].

The markets for carbon powders are unlikely to accommodate the production volumes required to satisfy global hydrogen demand. For example, producing turquoise hydrogen to meet today's hydrogen demand (∼100 MtH_2 yr^{-1}) would result in ∼300 MtC yr^{-1} solid carbon production; that is >10× larger than the current carbon black market (∼18 Mt yr^{-1}) [26, 27]. The production of primarily powdered CNTs is scaling to serve the battery electrode market, but is currently only ∼20 kt y^{-1} [37]. As a "carbon-first" approach, the multi-pass reactor produced CNTs with low diameter (∼10 nm) and high I_G:I_D ratio (up to 6) that naturally form bulk-materials within the reactor and can be densified for further property enhancement [16, 11, 38]. Using bulk CNT materials as replacements for materials like steel, aluminium and copper present the opportunity to not only increase CNT utilisation, but to realise additional CO_2-emission reductions by displacing CO_2-intensive materials. Further, the demonstration that multi-pass FCCVD can utilize biomass-derived methane offers a means for net sequestration of carbon from the atmosphere within useful materials.

Huntsman Corporation announced long-term goals to scale their FCCVD CNT process up to a 1 Mt(CNT) y^{-1} plant [39]. Assuming CNT and hydrogen production in the same proportion as the Pilot multi-pass process presented here, this plant would produce 330 kt(H_2) annually. 300 such plants could supply today's H_2 demand (∼100 Mt(H_2)), and consume ∼ 15% of global natural gas (see Supplementary Note 4 for further details).

The global capacity of FCCVD methane pyrolysis systems is currently small, though precise numbers are limited. Deploying this technology at scale presents a number of challenges. The first is the significant solid loss generated by the reactor. The pilot-scale reactor reduces the proportion of loss relative to lab-scale, but 15% of carbon is still lost. If such reactors are to process megatonnes of methane, the proportion of loss must reduce by orders of magnitude. Similarly, the pilot multi-pass reactor consumes ferrocene and thiophene at 25% and 7.5% the rate of methane, respectively. Working at the megatonne scale, this may become prohibitive and will demand innovation in terms of catalyst delivery and utilisation. There is scope for significant improvements in catalyst efficiency in FCCVD reactors since it has been estimated that <0.1% of catalyst particles grow CNTs [34]. Additionally, switching to elemental catalyst precursors may reduce costs.

A broader challenge is the significant (∼3%) leakage of methane from natural gas supplies [40], contributing ∼18% of total methane flux to the atmosphere [41]. Hydrogen that leaks into the atmosphere can also cause global warming [42], so any wide-scale deployment of methane pyrolysis must address both upstream methane and downstream hydrogen leakage. Conversely, the FCCVD process allows biogas conversion to functional carbons, allowing net removal of atmospheric carbon into functional materials [43]. Additionally, the diversion of natural gas away from combustion applications and into pyrolysis processes could reduce CO_2e emissions from existing infrastructure; without intervention these emissions alone will exceed the budget for 1.5 °C of global warming [44]. Overall, the multi-pass FCCVD process for co-production of bulk CNT materials and turquoise hydrogen could reduce greenhouse emissions, but considerable development is needed to deploy this technology on a meaningful scale.

Methods

Precursors

Gases were supplied by BOC: N4.5 (Zero grade) argon, methane, and CO_2, and N5.0 (CP grade) hydrogen and nitrogen. 98% purity ferrocene powder and >99% purity liquid thiophene were supplied by Sigma Aldrich. The MPbio precursor contained 67 vol% CH_4 and 33% CO_2 representative of unrefined landfill and biogas (47-70 vol% methane and 32-43 vol% CO_2) [28].

Dispensers

Gas flows were controlled by Alicat MC-Series mass flow controllers (MFCs) of the following maximum flow rates and calibration gases: process gas (5 SLPM, H_2), ferrocene carrier gas (1 SLPM, H_2), thiophene carrier gas (500 SCCM, H_2), methane (500 SCCM, CH_4), recycled process gas (2 SLPM, H_2), FTIR nitrogen purge (5 SLPM, N_2), and CO_2 (1 SLPM, CO_2).

Ferrocene was dispensed by flowing hydrogen carrier gas through a sublimation pack held at constant temperature, allowing dispensation rate calculations using vapour pressure data from Fulem (2013) [45]. Tubes carrying ferrocene vapour from the sublimation pack to the furnace were heated to 160 °C to prevent ferrocene condensing inside the pipework. Thiophene was dispensed by bubbling hydrogen through liquid thiophene cooled to 0.5 °C in an ice bath; dispensation rate was calculated using the Antoine Equation provided by NIST [46]. Fully saturated carrier gas was assumed for both precursors.

Reactor

CNTs were synthesised using the floating catalyst chemical vapour deposition (FCCVD) process first reported by Li et al. [19]. A collection chamber was fabricated by Mackworks Precision Engineering to allow continuous winding of CNT aerogel onto a rotating roller. Figure 3 shows a schematic of the reactor used in this study and Supplementary Figure 4 is a photograph of the reactor. The reactor could run in single-pass (SP) configuration with the recycle MFC closed and the SP/MP selector valve taking hydrogen from the exogenous gas supply. In single-pass configuration, all process gas exits the collection chamber through the water trap and bubbler.

Alternatively, the reactor could run in multi-pass (MP) configuration by closing the exogenous hydrogen supply and switching the SP/MP selector valve to accept recycled process gas. In multi-pass configuration, process gas from the collection chamber is pumped through the recycle MFC and back to the injector via the various MFCs and catalyst dispensers. During multi-pass operation, additional gas produced by the pyrolysis reaction left the reactor through the exhaust line. The exhaust line was fitted with a 2.3 kPa check valve to ensure air could not back-flow into the reactor. Precursor recipes are provided in Supplementary Table 1, along with an explanation of the differences between the single-pass and multi-pass recipes in Supplementary Note 5.

The reaction took place inside an alumina tube of 580 mm length × 45 mm ID × 50 mm OD. The reaction tube was heated inside a Carbolite Gero tube furnace with a set-point of 1300 - 1350 °C. Gases and precursors were injected through a 3 mm ID × 6.35 mm OD stainless steel tube that protrudes 80 mm into the reaction tube. Gases and products exited the reaction tube into a stainless steel collection chamber where the CNT aerogel was wound onto an aluminium roller of 50 mm diameter, rotating at approximately 60 rpm. A single CNT mat was collected for each experiment, made by winding many layers of aerogel on top of each other on the roller. A 500 mm × 6.35 mm stainless steel rod could be inserted through an Ultra-Torr fitting in the collection chamber and into the end of the reaction tube; this allowed CNT aerogel to be ‘fished’ from the reactor at the start of operation and in case winding was interrupted during an experiment.

Between experiments, the reactor was cooled down to ambient temperature and flushed with argon to remove flammable gases, and then flushed with air to make it safe to open and clean. CNT samples were removed from the collection chamber, and the reaction tube and collection chamber were cleaned of soot and other solid residues using acetone and isopropyl alcohol (IPA). Once clean, the reactor was sealed and heated up under a flow of air. Supplementary Note 6 describes the startup and shutdown procedure of the reactor in detail.

Measurement of CNT Production

Carbon nanotubes were collected from the reactor after each experiment in the form a mat collected on the roller, and material collected on the stainless steel ‘fishing rod’. Both samples were weighed using a microbalance (A&D BM-252). The CNT mass production for a given experiment was taken to be the sum of the mass of these two samples. The CNT mass production rate was calculated by dividing the CNT mass production by the experiment length, measured to the nearest minute using a Lenovo P50 laptop.

CNT Characterisation

Samples were cut from the CNT mats for characterisation. Raman spectroscopy was carried out using a Horiba XploRA PLUS Raman Microscope, using a 532 nm laser, 10% power, 450 – 850 nm grating, and 50x objective. Thermogravimetric analysis (TGA) was carried out using a Mettler Toledo TGA/DSC 2 under a flow of 25 SCCM of air. The samples were heated from 25 °C to 1000 °C at 5 °C per minute. Electrical conductivity measurements used a bespoke four-point probe jig connected to a milliohm meter (Aim-TTi BS407) to measure the resistance between three locations along the length of 100 mm x 10 mm strips of mat. The thickness of these strips was determined by averaging micrometer measurements taken at 3 positions along their length. Their mass was also measured using the microbalance, allowing density to be calculated. TEM samples were prepared by dispersing CNT samples in ethanol by sonication for $\sim$1 hour, until the ethanol was visibly slightly darker due to dispersed CNTs. The CNTs were then drip-cast onto copper TEM grids with holey carbon support films. TEM was carried out using Thermo Fisher Scientific Talos F200X G2 TEM.

Gas Measurements

During multi-pass operation the effluent flow rate was measured with an Alicat MW-Series low pressure drop mass flow meter (MFM) with full scale flow rate of 1000 SCCM, shown in the upper right of Fig. 3. Mass flow rate measurements were corrected for gas composition according to supplementary Note 7. During single-pass operation the MFM was replaced by a Sensidyne Gilibrator 2 with a 6 LPM standard flow cell. Hydrogen concentration in the effluent flow was measured using a V&F HSense mass spectrometer with accuracy equal to 3% of the measured value. The HSense was located downstream of the effluent MFM, shown at the top right of Fig. 3. Fourier transform infrared spectrometry (FTIR) was conducted using a Bruker Matrix II-MG FTIR with 5 m path length (0.5 cm^{-1} spectral resolution) tracking CH_4, C_2H_6, C_2H_4, C_2H_2, C_6H_6, H_2O, CO_2, CO. During multi-pass operation the FTIR was located downstream of the recycle MFC (Fig. 3). Recycled process gas was analysed in the FTIR and then returned to the reactor in a closed loop. The larger recycle flow provided quicker time-response ($\approx$ 20 s) than the smaller effluent flow, and the effluent and recycled process gasses have the same composition. To characterise the single-pass exhaust gases, the FTIR was positioned on the exhaust line.

Iron and Sulfur Content

Iron content was calculated from TGA residual mass by assuming the residual mass was Fe_2O_3, such that 69.94% of the residual mass would be the iron from the aerogel and the remaining 30.06% would be oxygen gained during the TGA experiment. Catalyst particle sulfur content was estimated to be 20 wt% based on the model of active catalyst particle chemistry presented by by Weller et al. (2019) [20]. The authors acknowledge that the specific role of sulfur in the process, and its concentration in catalyst particles, is not completely understood at the time of writing and this is an estimate.

Loss Quantities

Losses were calculated based on the total mass of each element injected into the process, minus the amount of that element measured leaving the reactor in the aerogel and effluent gas stream. This indicates the total mass that cannot be measured leaving the reactor. The assumption is made that any mass not leaving the reactor is accumulating inside the reactor as loss, for example on the walls of the reactor and in particle filters. This analysis allows quantitative analysis of the performance of the reactor regarding mass conversion into useful product vs mass converted in waste products, or loss. However, it cannot confirm the precise chemistry, mechanisms or location of loss inside the reactor.

Iron in the reactor forms solid particles which are removed from effluent and recycled gas flows by particle filters. Therefore all iron not accounted for in the aerogel must take the form of solid loss. The mass of sulfur loss is assumed to equal 20% of the mass of iron loss (assuming same nanoparticle chemistry as the catalyst in the aerogel). Hydrogen loss is assumed to take the form of hydrogenated surfaces on amorphous carbon loss, thus the ratio of of carbon loss to hydrogen loss is dependent on the chemistry of this amorphous carbon.

Sankey Diagrams

The Sankey diagrams in Fig. 4 collate the inputs for each process with data collected on the outputs and unmeasured values are calculated. The precursor input rates are provided in Supplementary Table 1. The input rates of elemental carbon, hydrogen, sulfur and iron are then calculated from these recipes by summing the contribution of each element from each of the precursors. The mass production rate of aerogel, effluent gas, and loss streams were calculated as described in the relevant sections above. Effluent H_2S is calculated by the mass of sulfur not accounted for in the aerogel and solid loss. Oxides were detected in the exhaust of the lab-scale process, primarily CO and H_2O. The source of the oxygen is believed to be leaks in the reactor's pipework, impurities in the feed gases, etching from the alumina (aliminium oxide) reaction tube, or some combination thereof. To simplify the Sankey diagrams, the fugitive oxygen was not included and the mass of "oxides" in the effluent flow account only for the mass of carbon and hydrogen bound in the oxide species. See Supplementary Note 4 for more detailed analysis of oxides in the effluent streams.

The Sankey diagrams representing the pilot-scale single pass process in Fig. 6a were constructed using data collected by the authors at the Tortech pilot-scale plant in Ma'alot Tarshiha and by characterising material produced by this process (Table 1); and, recipes and performance data provided by Tortech Nano Fibres. Supplementary Table 2 contains mass flow rates of precursors provided by Tortech, enabling the calculation of the elemental input rates. Production rate of CNTs is 30 g h^{-1} for this recipe; iron impurity in aerogel were measured using TGA and sulfur impurity was calculated at 20 wt% iron impurity, as above. The loss streams and effluent H_2S were also calculated as above. The mass flow of effluent methane is known from the methane conversion efficiency (85%), however concentration of other effluent gas species were not measured. The effluent concentrations of C_xH_y are assumed to be the same as in the lab scale single-pass process, oxide species are ignored. The ratio of solid hydrogen loss:carbon loss is assumed to match the lab-scale single-pass process, and any remaining hydrogen is assumed to leave the reactor in the effluent stream. The mass of effluent hydrogen not accounted for in species like H_2S, CH_4, and C_xH_y is assumed to be in the form of H_2, yielding the mass flow rate of effluent H_2 and defining the effluent flow rate. The mass of carbon loss is then iterated until the total mass of carbon in the aerogel, effluent and loss stream matches the carbon input, at which point all mass inputs and outputs of the reactor are balanced.

The effluent and loss flows shown with striped fills in Fig. 6a are calculated rather than measured, thus the relative distribution of loss between the solid and gas phase is based on calculation. However, the precursor flow rates and CNT production rates in Fig. 6a are measured values, and thus the sizes of the product and waste streams are based on measurements. The values for process efficiency and carbon yield are based on the size of these two streams and are thus based solely on measured values.

The Sankey diagram in Fig. 6b is constructed by combining the data collected for the pilot-scale single-pass process in Fig. 6a and the performance improvements demonstrated by the lab-scale multi-pass process. The performance improvements at pilot-scale cannot be as large as those seen in the lab because the pilot-scale single-pass process is already much more efficient (Table 1). The pilot-scale multi-pass process is designed to produce 30 g h^{-1} of CNT like the pilot-scale single-pass process, with the same quantities of iron and sulfur impurity. The exogenous hydrogen supply is completely removed assuming process gas will circulate in a closed loop as in the lab-scale multi-pass process. The flow rate of ferrocene is kept the same while thiophene flow is halved, inline with the lab-scale multi-pass process. 95% methane conversion efficiency is applied to the pilot-scale multi-pass process based on the 92% exhibited by the lab scale process. Effluent methane concentration is calculated based on this conversion efficiency. Effluent pyrolysis products are assumed to have same concentrations as in lab-scale multi-pass process and effluent oxides are ignored. Carbon loss is assumed to remain the same in the pilot-scale single-pass and multi-pass reactors, and the ratio of carbon loss: hydrogen loss is assumed to be same as in the lab-scale multi-pass reactor. The mass of iron loss is calculated as the mass of iron not accounted for in the aerogel and sulfur loss is calculated as 20% of the iron loss. The mass of effluent hydrogen and sulfur is calculated as the mass not accounted for in the aerogel and loss streams, providing the mass flow rate of effluent H_2S. Effluent H_2 is calculated as the mass of effluent hydrogen not accounted for in other effluent species, defining the effluent flow rate. The methane input into the process is then iterated until the inflows and outflows of carbon and hydrogen are balanced.

Efficiencies

CH_4 conversion is defined as

$$CH_4 \text{ conversion} = \frac{\dot{m}(CH_4, \text{injector}) - \dot{m}(CH_4, \text{exhaust})}{\dot{m}(CH_4, \text{injector})}, \tag{2}$$

measured during steady state operation. $\dot{m}(CH_4)$[injector] and $\dot{m}(CH_4)$[exhaust] are the mass flow rates of CH_4 in the injector and exhaust, respectively. CH_4 conversion describes the amount of methane converted into different species inside the reactor.

Hydrogen production efficiency in a multi-pass FCCVD reactor must consider the hydrogen liberated from ferrocene and thiophene along with the primary contribution from methane. H_2 production efficiency is thus defined as:

$$\text{H}_2 \text{ production efficiency} = \frac{\dot{m}(H_2, \text{exhaust})}{\dot{m}(H, \text{injector})}. \tag{3}$$

where $\dot{m}(H_2, \text{effluent})$ is the mass flow rate of H_2 leaving the reactor and $\dot{m}(H, \text{injector})$ is the mass flow rate of hydrogen injected into the reactor, during steady state operation.

Carbon yield is defined as:

$$\text{Carbon yield} = \frac{\text{Mass of carbon in aerogel (g)}}{\text{Total mass of carbon injected (g)}}, \tag{4}$$

during steady state operation. It describes the fraction of the total carbon injected into the system that is converted into useful carbon products.

Molar process efficiency is defined as

$$\text{Molar process efficiency} = \frac{\text{Amount of useful product (mol)}}{\text{Total precursor input (mol)}}, \tag{5}$$

measured during steady state. Note that the amount of product and precursors are measured in the number of atoms, rather than the number of molecules, such that molar efficiency described the number of atoms that are converted into useful products. In the single-pass process, useful product is limited to the carbon aerogel. In the multi-pass process, useful product includes both the aerogel and the effluent hydrogen gas. Molar carbon efficiency is calculated in the same way as the molar process efficiency, but only considers the moles of carbon product:

$$\text{Molar carbon efficiency} = \frac{\text{Amount of carbon product (mol)}}{\text{Total precursor input (mol)}}, \tag{6}$$

Mass-based process efficiency is defined similarly to molar process efficiency, but measures the mass of precursors and products rather than number of moles:

$$\text{Mass-based process efficiency} = \frac{\text{Mass of useful product (g)}}{\text{Total precursor input (g)}}. \tag{7}$$

Data Availability Statement

The authors declare that all data supporting the findings of this study are available within the paper and Supplementary Information files.

Acknowledgments

The authors wish to acknowledge the support of UKRI-EPSRC under grant reference EP/Y026098/1, under the Building a Green Future theme and the International Science Partnerships Fund as part of the Global Hydrogen Production Technologies (HyPT) Center, along with the Carbon Hub, and the Kavli Foundation Exploration Award in Nanoscience for Sustainability LS-2023-GR-51-2857. Additionally, Jack Peden would like to thank the Harding Distinguished Postgraduate Scholars Programme for funding his PhD. We would like to thank Tortech Nanofibres for allowing us to measure their process, and Q-Flo Limited for lending equipment and expertise in these experiments. We thank Felix Freebairn at Machworks Precision Engineering for designing and manufacturing the collection chamber that enabled continuous collection of CNT mat and recycling of the process gases in this reactor. Thanks to Luke Arnold, Barney Coles, and the rest of the technical staff at the Cambridge University Department of Engineering who were integral to keeping these experiments running smoothly. The Talos TEM used in this study was funded through the EPSRC Underpinning Multi-User Equipment Call (EP/P030467/1) and was expertly operated by Heather Greer.

Author Contributions Statement

The authors made the following contributions to this publication:

Jack Peden developed the final multi-pass reactor configuration used in this study, conceived of experiments use to evaluate the performance of the reactor, performed experiments throughout this study, analysed the data presented in this study, and created the figures and wrote the paper.

Dr James Ryley contributed to the development of the multi-pass reactor and performed experiments and data analysis for this study, particularly the operation of the FTIR and analysis of data to obtain accurate concentration measurements from the IR spectrum.

Dr Jeronimo Terrones contributed to the development of the multi-pass reactor.

Dr Fiona Smail conceived of the original multi-pass/ recycling reactor and contributed to its development.

Professor James Elliot provided valuable revisions to the original manuscript and contributed TGA analysis tools to this project.

Professor Alan Windle provided invaluable guidance and vision to transform what was a CNT synthesis process into a hydrogen production process.

Professor Adam Boies was the principle investigator in this project, conceiving of the multi-pass reactor and guiding its development, contributing Raman analysis tools, and substantially improved and revised the paper and figures many times.

Competing Interests Statement

The authors declare the following competing interests:

J.P. was previously employed by and Adam Boies has previously served as a consultant for Q-Flo Limited, a commercial entity with an interest in FCCVD technology succeeding. All other authors declare no competing interests.

Tables

Table 1: Process performance data and CNT characteristics of the 5 lab scale processes (SP, MP, MPbio, SP2, and MP2), along with the pilot-scale single-pass process (Pilot SP) and the modelled pilot-scale multi-pass (Pilot MP) process. ”—” represent data points not obtained in this study.

	SP	MP	MPbio	SP2	MP2	Pilot SP	Pilot MP
CNT mass production (g/hr)	0.132	0.165	0.0995	0.046	0.077	30.0	30.0
Carbon content (%)	64.41	75.53	58.89	78.33	85.37	95.02	95.02
Iron content (%)	29.66	20.39	34.26	18.06	12.19	4.15	4.15
Raman G/D	1.54	1.41	1.79	5.87	6.04	3.58	3.58
Electrical conductivity (S/m)	3643	1593	4165	63669	35470	—	—
Specific conductivity (S·m^2/kg)	26.74	11.48	21.87	233.2	213.9	—	—
Density (kg/m^3)	137.9	139.1	190.4	273.0	166.1	—	—
Methane conversion (%)	27.20	91.90	95.44	—	—	85.0	95.0
Hydrogen production efficiency (%)	0	54.15	32.99	0	—	0	87.64
Carbon yield (%)	2.38	20.76	9.61	1.37	18.24	60.0	79.14
Molar process efficiency (%)	0.100	44.69	27.20	0.037	—	1.48	85.18
Molar carbon efficiency (%)	0.100	5.36	3.23	0.037	4.21	1.48	79.22
Mass process efficiency (%)	0.806	23.17	7.95	0.34	15.98	13.60	75.00
Volumetric productivity (kg/m^3·h)	0.147	0.296	0.179	0	—	3.333	4.384
CNT volumetric productivity (kg/m^3·h)	0.147	0.183	0.111	0.051	0.09	3.333	3.333
H_2 volumetric productivity (kg/m^3·h)	0	0.113	0.069	0	—	0	1.051

References

[1] Schemme, S. *et al.* H2-based synthetic fuels: A techno-economic comparison of alcohol, ether and hydrocarbon production. *International Journal of Hydrogen Energy* **45**, 5395–5414 (2020). URL `https://www.sciencedirect.com/science/article/pii/S0360319919318580`.

[2] Madadi Avargani, V., Zendehboudi, S., Cata Saady, N. M. & Dusseault, M. B. A comprehensive review on hydrogen production and utilization in North America: Prospects and challenges. *Energy Conversion and Management* **269**, 115927 (2022). URL `https://www.sciencedirect.com/science/article/pii/S0196890422007233`.

[3] Henry, A., Prasher, R. & Majumdar, A. Five thermal energy grand challenges for decarbonization. *Nature Energy* **5**, 635–637 (2020). URL `https://www.nature.com/articles/s41560-020-0675-9`. Publisher: Nature Publishing Group.

[4] IEA. Global hydrogen demand in the Net Zero Scenario, 2022-2050 – Charts – Data & Statistics (2023). URL `https://www.iea.org/data-and-statistics/charts/global-hydrogen-demand-in-the-net-zero-scenario-2022-2050`.

[5] Diab, J., Fulcheri, L., Hessel, V., Rohani, V. & Frenklach, M. Why turquoise hydrogen will Be a game changer for the energy transition. *International Journal of Hydrogen Energy* **47**, 25831–25848 (2022). URL `https://www.sciencedirect.com/science/article/pii/S0360319922024983`.

[6] Ritchie, H. & Roser, M. Sector by sector: where do global greenhouse gas emissions come from? *Our World in Data* (2024). URL `https://ourworldindata.org/ghg-emissions-by-sector`.

[7] Rahimi, N. *et al.* Solid carbon production and recovery from high temperature methane pyrolysis in bubble columns containing molten metals and molten salts. *Carbon* **151**, 181–191 (2019). URL `https://www.sciencedirect.com/science/article/pii/S000862231930510X`.

[8] Lamy, C. & Millet, P. A critical review on the definitions used to calculate the energy efficiency coefficients of water electrolysis cells working under near ambient temperature conditions. *Journal of Power Sources* **447**, 227350 (2020). URL `https://www.sciencedirect.com/science/article/pii/S0378775319313436`.

[9] Muradov, N. Hydrogen via methane decomposition: an application for decarbonization of fossil fuels. *International Journal of Hydrogen Energy* **26**, 1165–1175 (2001). URL `https://www.sciencedirect.com/science/article/pii/S0360319901000738`.

[10] Qian, J. X. *et al.* Methane decomposition to pure hydrogen and carbon nano materials: State-of-the-art and future perspectives. *International Journal of Hydrogen Energy* **45**, 15721–15743 (2020). URL `https://www.sciencedirect.com/science/article/pii/S0360319920314567`.

[11] Zhang, X. *et al.* Simultaneously Enhanced Tenacity, Rupture Work, and Thermal Conductivity of Carbon Nanotubes Fibers by Increasing the Effective Tube Contribution. *Science Advances* **8**, eabq3515 (2022). URL `http://arxiv.org/abs/2204.04468`. ArXiv:2204.04468 [cond-mat].

[12] Behabtu, N. *et al.* Strong, Light, Multifunctional Fibers of Carbon Nanotubes with Ultrahigh Conductivity. *Science* **339**, 182–186 (2013). URL `https://www.science.org/doi/full/10.1126/science.1228061`. Publisher: American Association for the Advancement of Science.

[13] Gspann, T. S. *et al.* High thermal conductivities of carbon nanotube films and micro-fibres and their dependence on morphology. *Carbon* **114**, 160–168 (2017). URL `https://www.sciencedirect.com/science/article/pii/S0008622316310752`.

[14] Laurent, C., Flahaut, E. & Peigney, A. The weight and density of carbon nanotubes versus the number of walls and diameter. *Carbon* **48**, 2994–2996 (2010). URL `https://www.sciencedirect.com/science/article/pii/S0008622310002617`.

[15] Taylor, L. W. *et al.* Improved properties, increased production, and the path to broad adoption of carbon nanotube fibers. *Carbon* **171**, 689–694 (2021). URL `https://www.sciencedirect.com/science/article/pii/S0008622320307193`.

[16] Zhang, X. *et al.* Carbon nanotube fibers with dynamic strength up to 14 GPa. *Science* **384**, 1318–1323 (2024). URL `https://www.science.org/doi/10.1126/science.adj1082`. Publisher: American Association for the Advancement of Science.

[17] Fan, Z., Weng, W., Zhou, J., Gu, D. & Xiao, W. Catalytic decomposition of methane to produce hydrogen: A review. *Journal of Energy Chemistry* **58**, 415–430 (2021). URL `https://www.sciencedirect.com/science/article/pii/S2095495620307415`.

[18] Abánades, A. *et al.* Experimental analysis of direct thermal methane cracking. *International Journal of Hydrogen Energy* **36**, 12877–12886 (2011). URL `https://www.sciencedirect.com/science/article/pii/S0360319911017411`.

[19] Li, Y.-L., Kinloch, I. A. & Windle, A. H. Direct Spinning of Carbon Nanotube Fibers from Chemical Vapor Deposition Synthesis. *Science* **304**, 276–278 (2004). URL `https://www.science.org/doi/full/10.1126/science.1094982`. Publisher: American Association for the Advancement of Science.

[20] Weller, L. *et al.* Mapping the parameter space for direct-spun carbon nanotube aerogels. *Carbon* **146**, 789–812 (2019). URL `https://www.sciencedirect.com/science/article/pii/S0008622319300946`.

[21] Sun, E. *et al.* A semi-continuous process for co-production of CO2-free hydrogen and carbon nanotubes via methane pyrolysis. *Cell Reports Physical Science* **4**, 101338 (2023). URL `https://www.sciencedirect.com/science/article/pii/S2666386423001030`.

[22] Parmar, K. R., Pant, K. K. & Roy, S. Blue hydrogen and carbon nanotube production via direct catalytic decomposition of methane in fluidized bed reactor: Capture and extraction of carbon in the form of CNTs. *Energy Conversion and Management* **232**, 113893 (2021). URL `https://www.sciencedirect.com/science/article/pii/S0196890421000704`.

[23] Kutteri, D. A., Wang, I.-W., Samanta, A., Li, L. & Hu, J. Methane decomposition to tip and base grown carbon nanotubes and CO x -free H 2 over mono- and bimetallic 3d transition metal catalysts. *Catalysis Science & Technology* **8**, 858–869 (2018). URL `https://pubs.rsc.org/en/content/articlelanding/2018/cy/c7cy01927k`. Publisher: Royal Society of Chemistry.

[24] Wang, I.-W., Kutteri, D. A., Gao, B., Tian, H. & Hu, J. Methane Pyrolysis for Carbon Nanotubes and COx-Free H2 over Transition-Metal Catalysts. *Energy & Fuels* **33**, 197–205 (2019). URL `https://doi.org/10.1021/acs.energyfuels.8b03502`. Publisher: American Chemical Society.

[25] Silvy, R. A. P. & Arthur, D. J. System and Method for Synthesizing Carbon Nanotubes and Hybrid Materials Via Catalytic Chemical Deposition (2023). URL `https://patents.google.com/patent/US20230109092A1/en`.

[26] Glerum, M. W. J. & Boies, A. M. in *Chapter Three - Reactor processes for value added carbon synthesis and turquoise hydrogen* (eds Pelucchi, M. & Maestri, M.) *Advances in Chemical Engineering*, Vol. 61 of *Turquoise Hydrogen: An Effective Pathway to Decarbonization and Value Added Carbon Materials* 133–192 (Academic Press, 2023). URL `https://www.sciencedirect.com/science/article/pii/S0065237723000029`.

[27] Pasquali, M. & Mesters, C. We can use carbon to decarbonize—and get hydrogen for free. *Proceedings of the National Academy of Sciences* **118**, e2112089118 (2021). URL `https://www.pnas.org/doi/full/10.1073/pnas.2112089118`. Publisher: Proceedings of the National Academy of Sciences.

[28] Rasi, S. *Biogas composition and upgrading to biomethane.* Ph.D. thesis (2009). URL `https://jyx.jyu.fi/handle/123456789/20353`. Accepted: 2009-06-26T12:32:07Z ISBN: 9789513936181 Publisher: University of Jyväskylä.

[29] Guéret, C., Daroux, M. & Billaud, F. Methane pyrolysis: thermodynamics. *Chemical Engineering Science* **52**, 815–827 (1997). URL `https://linkinghub.elsevier.com/retrieve/pii/S0009250996004447`.

[30] Hoecker, C., Smail, F., Bajada, M., Pick, M. & Boies, A. Catalyst nanoparticle growth dynamics and their influence on product morphology in a CVD process for continuous carbon nanotube synthesis. *Carbon* **96**, 116–124 (2016). URL `https://linkinghub.elsevier.com/retrieve/pii/S0008622315302669`.

[31] Hoecker, C., Smail, F., Pick, M., Weller, L. & Boies, A. M. The Dependence of CNT Aerogel Synthesis on Sulfur-driven Catalyst Nucleation Processes and a Critical Catalyst Particle Mass Concentration. *Scientific Reports* **7**, 14519 (2017). URL `https://www.nature.com/articles/s41598-017-14775-1`. Number: 1 Publisher: Nature Publishing Group.

[32] Boies, A. M. *et al.* Agglomeration Dynamics of 1D Materials: Gas-Phase Collision Rates of Nanotubes and Nanorods. *Small* **15**, 1900520 (2019). URL `https://onlinelibrary.wiley.com/doi/abs/10.1002/smll.201900520`. _eprint: https://onlinelibrary.wiley.com/doi/pdf/10.1002/smll.201900520.

[33] Kateris, N., Kloza, P., Qiao, R., Elliott, J. A. & Boies, A. M. From Collisions to Bundles: An Adaptive Coarse-Grained Model for the Aggregation of High-Aspect-Ratio Carbon Nanotubes. *The Journal of Physical Chemistry C* **124**, 8359–8370 (2020). URL `https://pubs.acs.org/doi/10.1021/acs.jpcc.9b10479`.

[34] Reguero, V., Alemán, B., Mas, B. & Vilatela, J. J. Controlling Carbon Nanotube Type in Macroscopic Fibers Synthesized by the Direct Spinning Process. *Chemistry of Materials* **26**, 3550–3557 (2014). URL `https://doi.org/10.1021/cm501187x`. Publisher: American Chemical Society.

[35] Motta, M. *et al.* The parameter space for the direct spinning of fibres and films of carbon nanotubes. *Physica E: Low-dimensional Systems and Nanostructures* **37**, 40–43 (2007). URL `https://www.sciencedirect.com/science/article/pii/S1386947706003833`.

[36] Upham, D. C. *et al.* Catalytic molten metals for the direct conversion of methane to hydrogen and separable carbon. *Science* **358**, 917–921 (2017). URL `https://www.science.org/doi/full/10.1126/science.aao5023`. Publisher: American Association for the Advancement of Science.

[37] Temizel-Sekeryan, S., Wu, F. & Hicks, A. L. Global scale life cycle environmental impacts of single- and multi-walled carbon nanotube synthesis processes. *The International Journal of Life Cycle Assessment* **26**, 656–672 (2021). URL `https://doi.org/10.1007/s11367-020-01862-1`.

[38] Lee, D. *et al.* Ultrahigh strength, modulus, and conductivity of graphitic fibers by macromolecular coalescence. *Science Advances* **8**, eabn0939 (2022). URL `https://www.science.org/doi/10.1126/sciadv.abn0939`.

[39] Huntsman. Huntsman Miralon Product Portfolio (2024). URL `https://www.huntsman.com/products/detail/344/miralon`.

[40] Sherwin, E. D. *et al.* US oil and gas system emissions from nearly one million aerial site measurements. *Nature* **627**, 328–334 (2024). URL `https://www.nature.com/articles/s41586-024-07117-5`. Publisher: Nature Publishing Group.

[41] Jackson, R. B. *et al.* Increasing anthropogenic methane emissions arise equally from agricultural and fossil fuel sources. *Environmental Research Letters* **15**, 071002 (2020). URL `https://dx.doi.org/10.1088/1748-9326/ab9ed2`. Publisher: IOP Publishing.

[42] Ocko, I. B. & Hamburg, S. P. Climate consequences of hydrogen emissions. *Atmospheric Chemistry and Physics* **22**, 9349–9368 (2022). URL `https://acp.copernicus.org/articles/22/9349/2022/`. Publisher: Copernicus GmbH.

[43] Hanssen, S. V. *et al.* The climate change mitigation potential of bioenergy with carbon capture and storage. *Nature Climate Change* **10**, 1023–1029 (2020). URL `https://www.nature.com/articles/s41558-020-0885-y`. Publisher: Nature Publishing Group.

[44] Tong, D. *et al.* Committed emissions from existing energy infrastructure jeopardize 1.5 °C climate target. *Nature* **572**, 373–377 (2019). URL `https://www.nature.com/articles/s41586-019-1364-3`. Publisher: Nature Publishing Group.

[45] Fulem, M. *et al.* Recommended vapor pressure and thermophysical data for ferrocene. *The Journal of Chemical Thermodynamics* **57**, 530–540 (2013). URL `https://www.sciencedirect.com/science/article/pii/S0021961412003023`.

[46] NIST. Thiophene (2023). URL `https://webbook.nist.gov/cgi/cbook.cgi?ID=C110021&Mask=4#Thermo-Phase`.

[47] Stallard, J. C. *et al.* The mechanical and electrical properties of direct-spun carbon nanotube mats. *Extreme Mechanics Letters* **21**, 65–75 (2018). URL `https://www.sciencedirect.com/science/article/pii/S2352431618300130`.

[48] Ashby, M. *Material Property Charts* (Butterworth-Heinemann, 2011). URL `https://www.sciencedirect.com/science/article/pii/B9781856176637000047`. Pages: 57-96.

[49] Balasubramanian, M. *Composite Materials and Processing* (CRC Press, 2013). Google-Books-ID: 6rDMBQAAQBAJ.